Efficient Anisotropic Adaptive Discretization of the Cardiovascular System

O. Sahni [a,*] J. Müller [a] K.E. Jansen [a] M.S. Shephard [a]
C.A. Taylor [b]

[a] *Scientific Computation Research Center, Rensselaer Polytechnic Institute, 110 8th Street, Troy 12180 NY, USA*

[b] *James H. Clark Center, Room E350B, 318 Campus Drive, Stanford, CA 94305-5431, USA*

Abstract

We present an anisotropic adaptive discretization method and demonstrate how computational efficiency can be increased when applying it to the simulation of cardiovascular flow. A SUPG stabilized FE-method is used to solve the incompressible Navier-Stokes equations using linear elements. The anisotropic size field is determined from the recovered Hessian of the solution field. To perform mesh adaptation, a single mesh metric field is constructed for the whole cardiac cycle. Two alternative approaches are applied, one in which a metric field is constructed based on the average flow whereas in the other approach the metric field is obtained by intersecting metric fields computed at a number of specified instants during the cycle. We further demonstrate that controlling the mesh adaptation procedure in a way that maintains structured and graded elements near the wall leads to a more accurate wall shear stress computation. We apply the method to the case of a 3D branching vessel model. The efficiency of our approach is measured by analyzing the wall shear stress, a challenging but important quantity in the understanding of cardiovascular disease. The anisotropic adaptivity based on metric intersection achieves an order of magnitude reduction in terms of degrees of freedom when compared to uniform refinement for a given level of accuracy.

Key words: Anisotropic mesh adaptivity, mesh metric field, boundary layer mesh, computational blood flow, wall shear stress
PACS:

* Corresponding author
Email address: osahni@scorec.rpi.edu (O. Sahni).
URL: www.scorec.rpi.edu (O. Sahni).

1 INTRODUCTION

In recent years, the relationship between hemodynamic factors and arterial diseases has attracted numerous investigators to study arterial blood flow and wall shear stress (WSS) patterns. The direct application of such a relationship will help in surgical planning, in which patient-specific anatomic and physiologic information can be used to predict changes in blood flow for alternative surgical procedures [1].

Interesting challenges arise in blood flow simulations due to the transient and non-linear nature of the problem involving 3D geometries. Finite element (FE) methods provide a viable option for understanding the complex nature of blood flow and for obtaining relevant flow quantities, like WSS. The automatic and adaptive construction of properly configured anisotropic meshes is central to the ability to effectively perform these simulations.

In the procedures presented here, mesh adaptation is achieved by modifying the elements according to anisotropic mesh metrics defined by an error correction/indication procedure. Anisotropic mesh adaptation procedures reduce the number of elements (and degrees of freedom), leading to significant computational savings for a given level of accuracy.

Before describing our approach we review the current state of the art. One approach to control the error introduced due to discretization of the flow equations is to perform mesh adaptation that modifies the spatial discretization. One way to carry out mesh adaptation is by applying local mesh modification procedures dictated by the size field information based on *a posteriori* error estimators/indicators. Traditionally, the size field is based on scalar error information that allows for isotropic mesh adaptation generally resulting in equilateral elements.

The desired element size and orientation is significantly influenced by the characteristics of the solution field which in turn depends on the equations being solved, the initial and boundary conditions, and the geometry of the physical domain. Many physical problems exhibit strong anisotropic phenomena which introduces a desire for anisotropic elements, for example, boundary layers that form near walls in viscous flows or shock waves in high speed flows. In this scenario, an anisotropic mesh adaptation procedure capable of creating such elements is highly desirable to further increase the efficiency of the simulations.

Recent efforts to obtain anisotropic meshes have considered the mesh metric field to define the required mesh anisotropy. A mesh metric field allows one to invoke local mesh modification operations (or perform a remeshing process) in order to obtain elements that respect the required mesh anisotropy and in turn align the mesh with the solution anisotropy. Substantial progress has been made in the development of such procedures for three dimensional domains (see, [2] and references therein) including efforts on their application to a wide variety of physical problems in 2D [3–6] and 3D [7–9]. The mesh modification procedures have also been extended to handle 3D curved geometries [10], which makes the process amenable to blood vessels.

Although anisotropic meshes have been used in the field of fluid mechanics for some time, especially for cases with prior knowledge of boundary layers (see for example [11–15] and literature cited therein), adaptive specification of the size field for 3D problems has been achieved only in the past few years [7–9]. Most of the efforts carried out construct a mesh metric field based on the Hessian matrix of an appropriate solution variable.

Mesh adaptation procedures have only recently been utilized [16] in blood flow simulations. Most attempts to improve the simulation efficiency of hemodynamics by means of mesh adaptivity are limited to isotropic adaptation and steady flows, while cardiovascular flows are unsteady in nature and possess distinct directional features. In this article we have applied anisotropic mesh adaptation for pulsatile flow in realistic geometries chosen to demonstrate the major difficulties that are encountered in the process.

The cyclic transient phenomena in blood flows complicate the process of mesh adaptation as the flow features can propagate and vary, in terms of shape and/or intensity, with time. There are two possible approaches to perform mesh adaptation for such problems. In the first, the mesh is continually adapted according to the transient flow features. The second approach is to use a single adapted mesh for the entire unsteady flow cycle. The latter approach is a practical alternative for flows of pulsatile nature and therefore periodic in time. The single mesh adaptation process for the whole flow cycle can be based on different scenarios of flow conditions like the time averaged flow field, peak flow field over the cycle or spatially local peak flows. In this article, we apply two different adaptation strategies to obtain a single adapted mesh for the whole cardiac cycle. One approach is based on the average speed field as presented in [17] whereas in the other, size field information is constructed at certain instants of the cardiac cycle, based on the instantaneous speed field, and then combined into a single size field by using a metric intersection algorithm.

The organization of the paper is as follows. Section 2 introduces the numerical method that we use to solve hemodynamic flows and describes the computation of WSS. Section 3 presents the overall anisotropic mesh adaptation procedure. In this section we discuss the Hessian strategy and review the concept of a mesh metric field. We then provide the details of anisotropic mesh size field computation including a corrective mechanism of metric alignment at no-slip boundaries. Finally, we propose a method that accounts for the transient nature of the flow in the construction of the mesh metric field with the help of a metric intersection procedure. Section 4 considers the effects of mesh quality near the walls on WSS computation. In this section, we identify the mesh requirements in terms of element shape and gradation that will lead to more accurate computation of WSS. We provide a hybrid methodology that combines anisotropic adaptivity with a generalized advancing layers method to meet the desired requirements. Section 5 presents the application of different anisotropic adaptive strategies for cardiovascular flows. In the first part of this section, we analyze the efficiency of the two size field strategies; the average flow field based adaptivity and an alternative based on mesh metric intersection. We analyze the wall shear stress for a pulsatile flow case in a vessel bifurcating into symmetric branches. In the second part of this section, we demonstrate how mesh structure near the vessel walls affects the accuracy of WSS computation and hereby motivate the hybrid approach proposed in section 4.

2 BLOOD FLOW SIMULATION

This section presents the finite element formulation for the transient incompressible Navier-Stokes equation governing blood flow. We use a stabilized finite element formulation that has been shown to be robust, accurate and stable on a variety of flow problems (see for example [1] and [18]). In particular, we employ the streamline upwind/Petrov-Galerkin (SUPG) stabilization method introduced in [19]. The section also presents details on the numerical computation of wall shear stress.

2.1 Governing Equations

The governing equations for blood flow, assuming Newtonian constitutive behavior and rigid blood vessel walls, are the transient incompressible Navier-Stokes equations

$$u_{i,i} = 0, \tag{1}$$

$$\rho \dot{u}_i + \rho u_j u_{i,j} = -p_{,i} + \tau_{ij,j} + f_i. \tag{2}$$

The variables are: the velocity u_i, the pressure p, the density ρ, and the viscous stress tensor τ_{ij}. The summation convention is used throughout, i.e., sum on repeated indices. For incompressible, Newtonian flow the viscous stress tensor τ_{ij} is modeled by the symmetric strain rate tensor

$$\tau_{ij} = \mu(u_{i,j} + u_{j,i}), \tag{3}$$

where μ is the viscosity. Finally, f_i is a body force or source term, such as gravity. This term is typically neglected in arterial flow analysis. The above system of equations is supplemented with an appropriate set of boundary conditions that are prescribed on the model boundary of the blood vessels. The no-slip condition is imposed on the vessel walls that are assumed to be rigid and impermeable. A time varying velocity profile, based on physiological values, may be prescribed at the inlet. Constant pressure, resistance, or impedance boundary conditions can be prescribed at the outlet [20].

2.2 Flow Solver

Finite element methods are based on the weak form of the governing equations (1),(2) which is obtained by taking the $L^2(\Omega)$-inner product of the entire system with weight functions. Integration by parts is then performed to shift the spatial derivatives onto the weight functions. The diffusive term, pressure term and continuity equation are all integrated by parts. The diffusive term is integrated by parts to reduce continuity requirements, while the pressure term is integrated by parts to provide symmetry with the continuity equation which in turn is integrated by parts to provide discrete conservation of mass.

To derive the finite element discretization of the weak form of (1),(2), discrete weight and solution function spaces must be introduced. Let $\bar{\Omega} \subset \mathbf{R}^N$ represent the closure of the physical spatial domain (i.e., $\Omega \cup \Gamma$ where Γ is the boundary) in N dimensions; where only $N = 3$ is considered here. The boundary is decomposed into portions with natural boundary conditions, Γ_h, and essential boundary conditions, Γ_g, i.e., $\Gamma = \Gamma_g \cup \Gamma_h$. In addition, $H^1(\Omega)$ represents the usual Sobolev space of functions with square-integrable values and derivatives on Ω. Subsequently Ω is discretized into n_{el} finite elements, $\bar{\Omega}_e$. With this, one can define the discrete solution and weight function spaces for the semi-discrete formulation as:

$$\boldsymbol{\mathcal{S}}_h^k = \{\boldsymbol{v}|\boldsymbol{v}(\cdot,t) \in H^1(\Omega)^N, t \in [0,T], \boldsymbol{v}|_{x\in\bar{\Omega}_e} \in P_k(\bar{\Omega}_e)^N, \boldsymbol{v}(\cdot,t) = \boldsymbol{g} \,\text{on}\, \Gamma_g\}, \quad (4)$$

$$\boldsymbol{\mathcal{W}}_h^k = \{\boldsymbol{w}|\boldsymbol{w}(\cdot,t) \in H^1(\Omega)^N, t \in [0,T], \boldsymbol{w}|_{x\in\bar{\Omega}_e} \in P_k(\bar{\Omega}_e)^N, \boldsymbol{w}(\cdot,t) = \mathbf{0} \,\text{on}\, \Gamma_g\}, \quad (5)$$

$$\mathcal{P}_h^k = \{p|p(\cdot,t) \in H^1(\Omega), t \in [0,T], p|_{x\in\bar{\Omega}_e} \in P_k(\bar{\Omega}_e)\}, \quad (6)$$

$P_k(\bar{\Omega}_e)$ denoting the space of all polynomials defined on $\bar{\Omega}_e$, complete up to order $k \geq 1$. Let us emphasize that the local approximation space, $P_k(\bar{\Omega}_e)$, is the same for both the velocity and pressure variables. This is possible due to the stabilized nature of the formulation to be introduced below. These spaces represent discrete subspaces of the spaces in which the weak form is defined.

The stabilized formulation used in the present work is based on the formulation described in [1]. Given the spaces defined above, the semi-discrete Galerkin finite element formulation is applied to the weak form of the governing equations (1),(2) as: Find $\boldsymbol{u} \in \boldsymbol{\mathcal{S}}_h^k$ and $p \in \mathcal{P}_h^k$ such that

$$B_G(w_i, q; u_i, p) = 0, \tag{7}$$

$$\begin{aligned} B_G(w_i, q; u_i, p) = &\int_\Omega \{w_i \left(\rho \dot{u}_i + \rho u_j u_{i,j} - f_i\right) + w_{i,j} \left(-p\delta_{ij} + \tau_{ij}\right) - q_{,i} u_i\} \, d\Omega \\ &+ \int_{\Gamma_h} \{w_i \left(p\delta_{ij} - \tau_{ij}\right) n_j + q u_i n_i\} \; d\Gamma, \end{aligned} \tag{8}$$

for all $\boldsymbol{w} \in \boldsymbol{\mathcal{W}}_h^k$ and $q \in \mathcal{P}_h^k$. The boundary integral term arises from the integration by parts and is only carried out over the portion of the domain without essential boundary conditions. Since the standard Galerkin method is well known to be unstable for equal-order interpolation of the velocity and pressure, additional stabilization terms are introduced as follows: Find $\boldsymbol{u} \in \boldsymbol{\mathcal{S}}_h^k$ and $p \in \mathcal{P}_h^k$ such that

$$B(w_i, q; u_i, p) = 0, \tag{9}$$

$$\begin{aligned} B(w_i, q; u_i, p) = &B_G(w_i, q; u_i, p) \\ &+ \sum_{e=1}^{n_{el}} \int_{\bar{\Omega}_e} \{\tau_M (u_j w_{i,j} + q_{,i}/\rho) \mathcal{L}_i + \tau_C w_{i,i} u_{j,j}\} \, d\Omega_e \\ &+ \sum_{e=1}^{n_{el}} \int_{\bar{\Omega}_e} \{w_i \rho \overset{\Delta}{u}_j u_{i,j} + \hat{\tau} \mathcal{L}_j w_{i,j} \mathcal{L}_k u_{i,k}\} \, d\Omega_e, \end{aligned} \tag{10}$$

for all $\boldsymbol{w} \in \boldsymbol{\mathcal{W}}_h^k$ and $q \in \mathcal{P}_h^k$. We have used $\mathcal{L}_i$ to represent the residual of the ith momentum equation

$$\mathcal{L}_i = \rho \dot{u}_i + \rho u_j u_{i,j} + p_{,i} - \tau_{ij,j} - f_i. \tag{11}$$

The second line in the stabilized formulation, (10), represents the typical SUPG stabilization added to the Galerkin formulation for the incompressible set of equations (see [21]). The first term in the third line of (10) was introduced in [1] to overcome the lack of mass conservation introduced as a consequence of the momentum stabilization in the continuity equation. The second term on this line was introduced to stabilize this new advective term. The stabilization parameters are described in [18].

To summarize, we use the SUPG stabilized formulation for the transient incompressible Navier-Stokes equations, governing blood flow, that are discretized by linear finite elements, both for the pressure and the velocity field.

Stabilized finite element methods have been proven to be stable and higher-order accurate for linear symmetric advective-diffusive systems (model problem for the Navier-Stokes equations) in [22] and for the linearized incompressible Navier-Stokes equations in [21]. Error analysis in these references relate the global error estimates to interpolation estimates and show that the rate of convergence of the total error is the same as that of interpolation estimates in their respective, restricted cases. Error estimates for the full Navier-Stokes equations are not yet available.

To develop a discrete system of algebraic equations, the weight functions w_i and q, the solution variables u_i and p, and their time derivatives are expanded in terms of the finite element basis functions. Gauss quadrature of the spatial integrals results in a system of first-order, nonlinear differential-algebraic equations. Finally, this system of non-linear ordinary differential equations is discretized in time via a generalized-α time integrator [23], resulting in a non-linear system of algebraic equations. This system is in turn linearized with Newton's method which yields a linear algebraic system of equations that is solved (at each time step) and the solution is updated for each of the Newton iterations. The linear algebra solver of [24] is used to solve the linear system of equations.

2.3 Wall Shear Stress Computation

The wall shear stress can be defined in terms of the surface traction vector $\boldsymbol{t}$ whose components are given as:

$$t_i = (-p\delta_{ij} + \tau_{ij})\, n_j, \tag{12}$$

p denoting the pressure, τ_{ij} are the components of the viscous stress tensor and n_j are the components of the normal $\boldsymbol{n}$ to the surface. The WSS is then defined, on each point on the surface, as:

$$t_w = |\boldsymbol{t}_w| = |\boldsymbol{t} - (\boldsymbol{t} \cdot \boldsymbol{n})\boldsymbol{n}|, \tag{13}$$

that is, the magnitude of the traction vector's component in a plane tangential to the surface.

Traditionally the boundary quantities, also referred as wall quantities, like the viscous fluxes $\hat{\tau}_{in}$ $(= \tau_{ij} n_j)$, are evaluated by substituting the numerical derivatives of flow quantities into the definition of the fluxes. However, instead of computing the viscous flux in this way (i.e., by differentiating the velocity) a more accurate and globaly conservative computation can be made by introducing a modified finite element formulation with an auxiliary flux field for the boundary flux on the portion with essential boundary conditions, Γ_g

(see [25, page 107], [26]). Taking $\hat{\tau}_{in}$ as the unknown (discrete) viscous flux, the modified formulation which derives from the discrete weak formulation (10) is: Find $\boldsymbol{u} \in \boldsymbol{\mathcal{S}}_h^k$, $p \in \mathcal{P}_h^k$ and $\hat{\tau}_{in} \in \boldsymbol{W}_h^k - \boldsymbol{\mathcal{W}}_h^k$ such that

$$B_{mod}(w_i, q; u_i, p) = 0, \tag{14}$$

$$\begin{aligned} B_{mod}(w_i, q; u_i, p) = B(w_i, q; u_i, p) & \\ + \int_{\Gamma_g} \hat{w}_i(-\,\hat{\tau}_{in})\, d\Gamma & \qquad \forall \hat{\boldsymbol{w}} \in \boldsymbol{W}_h^k - \boldsymbol{\mathcal{W}}_h^k. \end{aligned} \tag{15}$$

Note that the above problem splits into two subproblems:

$$B(w_i, q; u_i, p) = 0 \qquad \forall \boldsymbol{w} \in \boldsymbol{\mathcal{W}}_h^k, \tag{16}$$

$$\int_{\Gamma_g} \hat{w}_i \hat{\tau}_{in}\, d\Gamma = B(\hat{w}_i, q; u_i, p) \qquad \forall \hat{\boldsymbol{w}} \in \boldsymbol{W}_h^k - \boldsymbol{\mathcal{W}}_h^k, \tag{17}$$

where $\boldsymbol{W}_h^k$ is the discrete function space spanned by the basis functions including the ones omitted to satisfy the homogenous essential boundary conditions. Let η denote the set of all degrees of freedom (*dof*) and η_g be the subset corresponding to the ones located on Γ_g. $\boldsymbol{\mathcal{W}}_h^k$ spans all the basis functions associated with $\eta - \eta_g$, as:

$$\boldsymbol{\mathcal{W}}_h^k = span\{\boldsymbol{N}_A\}_{A \in \eta - \eta_g}, \tag{18}$$

where $\boldsymbol{N}_A$ is a basis function associated with *dof* $\boldsymbol{d}_A$. Now, $\boldsymbol{W}_h^k$ can be expressed as:

$$\boldsymbol{W}_h^k = \boldsymbol{\mathcal{W}}_h^k \bigoplus span\{\boldsymbol{N}_A\}_{A \in \eta_g}. \tag{19}$$

This technique is often referred as the *consistent* boundary-flux calculation technique and it is constructed to satisfy the conservation properties, see, e.g., [27, pages 42–44] and [26]. The auxiliary problem (17) is solved for the boundary flux after the original problem (16) as a post-processing step (i.e., if $\boldsymbol{u}$ ($\in \boldsymbol{\mathcal{S}}_h^k$) is already determined by (16), then the right-hand side of (17) is completely determined). The flux is expressed in terms of the basis functions associated with η_g. The integrals in (17) exist only over the elements touching Γ_g, due to the compact support of basis functions, making the auxiliary problem inexpensive.

The traction vector $\boldsymbol{t}$ can be computed once $\hat{\tau}_{in}$ is known, which in turn can be used to compute the WSS as defined in (13). The remaining step is the computation of the normal $\boldsymbol{n}$ at boundary nodes. Noting the normal is not uniquely defined at nodes on curved boundaries (i.e., vessel walls) because of the C^0 mesh elements, the final task is to find an appropriate normal. In this work, we use basis function weighted normals as described in [27, pages 542–544].

3 ANISOTROPIC ADAPTIVE PROCEDURE

The accuracy of a numerical solution depends on the spatial discretization of the physical domain, i.e., on the process of subdividing the domain into a finite number of elements, also referred to as the mesh. In general, the desired element sizes in different directions are influenced by the physical and geometric features of the problem which can vary significantly. In many physical problems, including blood flow, the solution exhibits strong anisotropic features creating a demand for elements which are aligned with the solution's anisotropy. In realistic cases such information, required to compute the desired solution field to an acceptable level of accuracy, is unknown *a priori*. An efficient approach to overcome this difficulty is to apply an iterative adaptive procedure where the errors introduced due to spatial discretization are controlled within a specified tolerance. An anisotropic adaptive procedure modifies the mesh in a way such that the local mesh resolution becomes adequate in all directions.

In this section, we describe the anisotropic adaptive procedure that we employ. We describe the basis for the Hessian strategy, a method suited when using linear finite elements, and review the concept of mesh metric tensors which is used to represent the desired mesh anisotropy. We then provide the details of the anisotropic mesh size field computation. We also present a technique to align mesh metrics at no-slip boundaries. Finally, we sketch how time dependence of the solution can be included in the adaptive process by combining mesh metric fields that are obtained at specified instants during a cardiac cycle, hereby avoiding mesh adaptation after each single time step.

3.1 General Components

An adaptive method involves a feed-back process that evaluates the quality of the computed solution using *a posteriori* error estimation. To control the discretization errors mesh modification procedures are applied to change the local mesh resolution. The key ingredients of an adaptive meshing method include:

- *A posteriori* error estimation/indication: Estimating and/or obtaining an indication of the discretization error based on the quality of the computed solution. See [28] or [29] for a survey.
- Size field construction: Transformation of the error information into a size field information that describes the desired mesh resolution over the domain.
- Modifying strategy: Altering the mesh based on the size field information using local mesh modifications [30,31] or global remeshing [32,33].

The above components are general enough to include anisotropic mesh adaptation techniques provided each of them incorporates appropriate directional information. The remainder of this section elaborates on these key components, except the last item which has been described in [2,34].

3.2 Hessian Strategy

To obtain directional information of the error we use the Hessian strategy [35], a method where the field's second derivatives are used to extract information on the error distribution. The Hessian can be computed from any component of the solution field and a scalar, such as speed or density is usually chosen. This directional information is converted into a mesh metric field which prescribes the desired element size and orientation. Recall that a function which is sufficiently smooth can be expanded into a Taylor series. When trying to interpolate that function with a piecewise linear function, the interpolation error will have a lowest order error term proportional to the second derivatives of the function, which covers a large portion of the discretization error [36].

The interpolation error $\|e\|_{\infty,K}$ in 3D in the L_∞ norm defined on an element K, given the solution is sufficiently regular, then can be measured as follows [37]:

$$\|e\|_{\infty,K} \leq c_1 \max_{x\in K} \max_{\boldsymbol{v}\subset K} \langle \boldsymbol{v}, |H(x)|\boldsymbol{v}\rangle, \tag{20}$$

$$\leq c_1 \max_{x\in K} \max_{\boldsymbol{e}\in E_K} \langle \boldsymbol{e}, |H(x)|\boldsymbol{e}\rangle, \tag{21}$$

where c_1 is a constant independent of element parameters, $\boldsymbol{v}$ is any vector contained in the element, E_K is the set of element edges and $|H|$ is the absolute value of the Hessian matrix of the solution (i.e., consists of absolute eigenvalues). To obtain such error estimates over the domain in different norms see references [35,38,39].

The Hessian strategy involves the computation of the symmetric matrix of second derivatives that can be decomposed as $H = \mathcal{R}\Lambda\mathcal{R}^T$, where $\mathcal{R}$ is the eigenvector matrix and $\Lambda = diag(\lambda_k)$ is the diagonal matrix of eigenvalues ($k = 1, 2, 3$ in 3D). The directions associated with the eigenvectors $\boldsymbol{p}_k$ are referred as principal directions and the eigenvalues λ_k are then equivalent to the second derivatives along the local principal directions. The strategy is based on the idea that a high magnitude of an eigenvalue implies a high error in the direction associated with the corresponding eigenvector, so a small element size would be desired in this direction. Conversely, a low eigenvalue magnitude in a particular eigendirection suggests that the element size can be large in this direction.

3.3 Mesh Metric Field

To perform anisotropic mesh adaptation requires a way to define the desired element size distribution over the domain. Mesh metric tensors are used to represent a size field defining the desired mesh anisotropy at a point (see for example, [40]). A mesh metric field is used to represent the desired size field as a second order tensor at each point of the domain. The mesh metric tensor at any point P in the domain is defined as a symmetric positive definite matrix $\mathcal{M}$. The associated quadratic form $\langle \boldsymbol{x}, \mathcal{M}\boldsymbol{x} \rangle = 1$, defines a mapping of an ellipsoid in the physical space into a unit sphere in the *transformed/metric* space. In other words, any vector $\boldsymbol{x}$ at point P assumes a unit value where distances are measured in the metric space.

The stated goal of the mesh adaptation algorithm is to yield a mesh with regular elements in the metric space where each edge $\boldsymbol{e}$ must satisfy the following relation:

$$\langle \boldsymbol{e}, \mathcal{M}\boldsymbol{e} \rangle = 1. \tag{22}$$

For further details on mesh modifications and element quality measures in the transformed space see references [2,34]. The same references also provide the details of the discretization of the mesh metric field over the domain along with its implementation.

3.4 Size Field Computation

A crucial step in the process is the construction of a size field based on the Hessian that can be input to the mesh adaptation module. The key point in the construction of a size field is to attempt to uniformly distribute the estimated error in all directions. To achieve a suitable mesh resolution in different directions, a uniform distribution of local errors is applied in the principal directions which leads to $h_k^2|\lambda_k| = \epsilon$, where ϵ is the user specified tolerance for the error and h_k is the desired size in the kth principal direction.

To compute the Hessian matrix we reconstruct the second derivatives at each node by using the derivative information of the computed solution from the patch S of all elements K surrounding a node. In the first step we recover the gradient at node i by taking the volume weighted average of gradients on elements in the patch S_i. This is equivalent to a lumped-mass approximation of a least squares reconstruction of the gradient for linear elements. The same procedure is applied to each term of second derivatives to obtain the recovered Hessian matrix. Care must be taken with the reconstruction on boundary nodes as the above procedure is less accurate for these nodes. A simple extrapolation technique is applied to project the interior values onto the nodes that lie on the domain boundary.

A mesh metric tensor is then obtained at each node by calculating a scaled eigenspace of the recovered Hessian matrix as $\overline{\mathcal{M}} = \mathcal{R}\bar{\Lambda}\mathcal{R}^T$, where $\mathcal{R}$ is the eigenvector matrix and $\bar{\Lambda} = \Lambda/\epsilon$ is the diagonal matrix of scaled eigenvalues. Truncation values h_{min} and h_{max} for mesh sizes are specified to limit the eigenvalues. One reason for truncating the element size, in terms of edge lengths, is to avoid singular metrics. For example, it is necessary to apply h_{max} in case an eigenvalue is zero (or close to zero) in the direction where the solution does not vary. The modified eigenvalues of the Hessian matrix then become:

$$\tilde{\lambda}_k = \min(\max(\epsilon^{-1}|\lambda_k|, \frac{1}{h_{max}^2}), \frac{1}{h_{min}^2}), \qquad (k = 1, 2, 3). \tag{23}$$

The final mesh metric field is constructed at each node through multiplication of the diagonal matrix of modified eigenvalues $\tilde{\Lambda} = diag(\tilde{\lambda}_k)$ with the matrix $\mathcal{R}$ of eigenvectors: $\mathcal{M} = \mathcal{R}\tilde{\Lambda}\mathcal{R}^T$.

3.5 Metric Alignment at No-Slip Boundaries

The numerically computed second derivatives near boundaries are of limited accuracy leading to a situation where the mesh metric tensors constructed at nodes with a no-slip boundary condition are not always well aligned with the correct directions. When fluid flows past a solid wall, one of the principle directions of the Hessian is usually aligned with the normal to the solid wall. Furthermore, in most cases, this normal direction has the highest eigenvalue (smallest size request). We can exploit this physical property and reduce our alignment error by aligning this principal direction (ordered as $\boldsymbol{p}_1$ without loss of generality) with the local surface normal vector $\boldsymbol{n}$. The plane containing the other two principal directions ($\boldsymbol{p}_2$ and $\boldsymbol{p}_3$) will approximate the tangential plane. Then, the principal direction (say, $\boldsymbol{p}_2$) associated with the next largest eigenvalue (λ_2) is projected on the tangential plane together with its size (h_2), see Fig. 1, as follows:

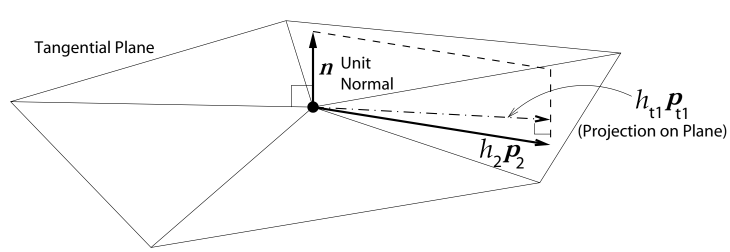

Fig. 1. Projection of vector $h_2\, \boldsymbol{p}_2$ on tangential plane.

$$\boldsymbol{p}_{t1} = (\boldsymbol{p}_2 - (\boldsymbol{p}_2 \cdot \boldsymbol{n})\boldsymbol{n}) / \|\boldsymbol{p}_2 - (\boldsymbol{p}_2 \cdot \boldsymbol{n})\boldsymbol{n}\|, \tag{24}$$

$$h_{t1} = |(\boldsymbol{p}_2 \cdot \boldsymbol{p}_{t1})|\, h_2, \tag{25}$$

where $\boldsymbol{p}_{t1}$ is the normalized projection of $\boldsymbol{p}_2$ onto the tangential plane and h_{t1} is the desired size in the direction of the projected vector $\boldsymbol{p}_{t1}$. Here, we essentially remove the part of the vector along the surface normal $\boldsymbol{n}$. The third principal direction $\boldsymbol{p}_{t2}$ also lies on the tangential plane and is orthogonal to $\boldsymbol{n}$ and $\boldsymbol{p}_{t1}$, i.e., $\boldsymbol{p}_{t2} = \boldsymbol{n} \times \boldsymbol{p}_{t1}$. The desired size h_{t2} in this direction is

$$h_{t2} = |(\boldsymbol{p}_3 \cdot \boldsymbol{p}_{t2})|\, h_3. \tag{26}$$

Similarly, the desired size in the direction of $\boldsymbol{p}_1$ can be projected onto the surface normal $\boldsymbol{n}$ as $h_n = |(\boldsymbol{p}_1 \cdot \boldsymbol{n})|\, h_1$. The aligned mesh metric then can be constructed based on the three new principal directions (i.e., $\boldsymbol{n}$, $\boldsymbol{p}_{t1}$ and $\boldsymbol{p}_{t2}$) and corresponding sizes (i.e., h_n, h_{t1} and h_{t2}).

3.6 Including Time Dependence: Intersecting Instantaneous Metrics

The mesh metric construction and subsequent anisotropic adaptation of the mesh is of non-trivial cost. Furthermore, the error (and computational cost) induced in the process of transferring the solution from the original to the adapted mesh must be considered. It is sometimes prudent to consider alternatives, wherein the mesh is adapted less frequently. In the case of pulsatile flow, the resulting flow is periodic in time, at least when phase averaged over a number of cycles. In this scenario one can construct an adapted mesh that would be appropriate for the entire cycle.

After making the decision to adapt once rather than at each flow step, the selection of a solution field (or fields) to be used to extract size field information remains. Clearly, one poor choice would be to select one time step since we anticipate significant variation in the size field over the cardiac cycle. An economical alternative is to consider the average flow over an integer number of cardiac cycles, which was also pursued in [17]. Meshes with significant anisotropy were created and shown to efficiently predict wall shear stress for a porcine aorta model. The downside to such an approach is that there is, in general, no guarantee that the size field requirements of any given step can be extracted from the average flow field. An alternative strategy is to construct a mesh metric field at several pre-defined instants of the cycle and then combine these metric fields into a single one that is the inner envelope of the set of mesh metrics.

The goal is to find a unique mesh metric tensor that is obtained by intersecting all the instantaneous metric tensors at each node. To define the intersection of two mesh metric tensors we employ the fact that each of them can be geometrically represented by an ellipsoid. Consider two mesh metric tensors $\mathcal{M}_1$ and $\mathcal{M}_2$ represented by their corresponding ellipsoids $\mathcal{E}_{\mathcal{M}_1}$ and $\mathcal{E}_{\mathcal{M}_2}$ we can define the resulting intersected metric tensor $\mathcal{M}$ as the one which can be geometrically represented by the maximum volume ellipsoid $\mathcal{E}_{\mathcal{M}_1 \cap \mathcal{M}_2}$ that is contained within the intersection of ellipsoids $\mathcal{E}_{\mathcal{M}_1}$ and $\mathcal{E}_{\mathcal{M}_2}$, for details see [37,41].

In practice the intersection of metrics is achieved by the simultaneous reduction or diagonalization of two quadratic forms which is a valid operation since both the tensors are positive definite. We illustrate the procedure from a geometric point of view in Fig. 2. It can be shown that this process allows one to compute a common basis for the two quadratic forms that can be used to determine the ellipsoid with maximum volume contained in the geometric intersection of the two candidate ellipsoids. The ellipsoid represented by the final intersected metric is the one with maximum volume contained in the common volume of all the candidates and therefore respects the size requirements of different time steps. From an implementation perspective, the

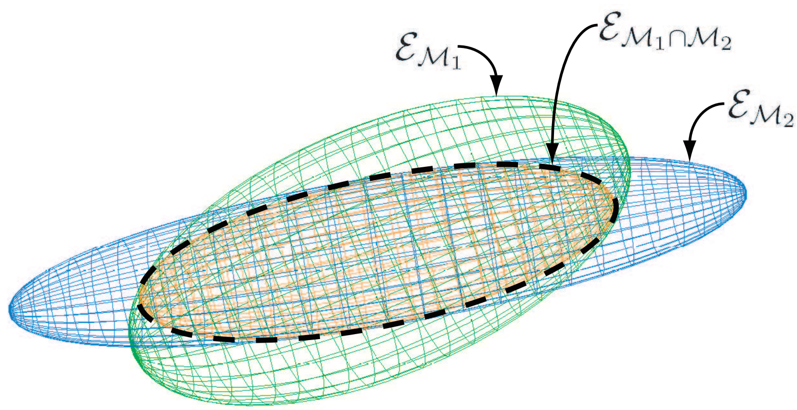

Fig. 2. Intersection of mesh metric tensors represented by ellipsoids.

intersection procedure is sequentially performed for all instantaneous fields chosen (in practice this is a subset of the timesteps in a given period). This involves construction of a mesh metric field for each selected instantaneous field and combining it with the one obtained through intersection of all the previous selected instantaneous fields.

4 MESH ADAPTATION IN BOUNDARY LAYERS

The mesh metric field developed in the previous section can be combined with mesh modification procedures (see, [2]) but the resulting meshes can be expected to produce wall shear stress fields which have some inaccuracies. We demonstrate that forcing structured layers of elements near the wall results in much smoother wall shear stress fields. In this section, we first review the two existing classes of anisotropic boundary layer meshing strategies (generalized advancing layers and anisotropic adaptivity), noting their strengths and weaknesses, and then propose a hybrid of the two approaches that captures the strengths of each.

4.1 Generalized Advancing Layers

Mesh generation for viscous flow simulations has been tackled and addressed by many researchers (see, [11] and references therein). The main idea of the technique, referred to as *generalized advancing layers method*, is to inflate the surface mesh into the volume along the local surface normals. The inflation process is generalized by making it flexible to be able to handle geometries with sharp corners or edges by creating *blend* elements. Such a mesh possesses structure in the direction normal to the walls by creating triangular prisms.

In some sense, this approach is a natural extension of the structured grid boundary layer mesh generators to unstructured grids. Many of the favorable attributes of structured grid meshes (control of the rate of change in element size along normals, high-quality/high-aspect ratio elements, orthogonal elements at the boundary) were inherited by this approach. This filling of the domain bounded by exterior no-slip surfaces (e.g., vessel walls) with stretched elements and special treatment of intersecting surfaces at interior edges/corners with high folding angle and hence, poorly defined normals often results in meshes with elements of unacceptable sizes for the flow features. Perhaps of even greater concern is that this approach also inherited a major deficiency of its structured grid predecessor: the need to specify the surface element size and the distribution of points normal to the surface (e.g., spacing of first point off of the wall, total thickness of the layers, number of layers) *a priori*.

4.2 Anisotropic Adaptivity

For real applications involving complex geometries, the flow features are unknown making an *a priori* specification of the boundary layer size field impractical. To address this difficulty, metric-based anisotropic adaptivity was developed. The advantage of this approach is that no *a priori* size information is required. The anisotropic adaptivity described heretofore makes no effort to create and/or preserve orthogonality of short edges to the boundary. Although this issue has only a minor influence on the flow variables, it has a much larger impact upon the wall shear stress computation.

The two boundary layer discretization approaches are illustrated in Fig. 3. Shown are the clip planes of two meshes of a bypassed porcine aorta model; the mesh shown on the left was generated by employing the advancing layers method (for three layers) whereas the mesh on the right has been obtained through an anisotropic mesh size field determined using the procedure described earlier. The section of the mesh has been chosen to exemplify the issues that exist in both the approaches in a general way including the situation where a corner is present. While the adapted case has captured the trend of small, isotropic elements near the corner, it has done so with considerably less smoothness in element size variation when compared to the advancing layers approach. One can further see that it has created considerably more anisotropic elements away from the corner, underscoring the impracticality of *a priori* determination of the mesh sizes required by the advancing layers approach.

We have observed that the advancing layers mesh, due to its structured nature, is capable of delivering a WSS field that can be characterized as being smoother with less fluctuations. The thicknesses of each of the layers have been pre-defined and do not match the sizing requirement for an adequate resolution of the flow field. The difficulty of using a pre-defined advancing layers mesh in our blood flow application is further substantiated by considering the instantaneous flow profile in Fig. 3 which indicates strong variation of near wall gradients. The anisotropically adapted mesh on the other hand integrates the desired size field and therefore reflects the attempted overall reduction of the discretization error by distributing it equally in all directions over the entire domain. As a remedy we propose a hybrid approach which combines the

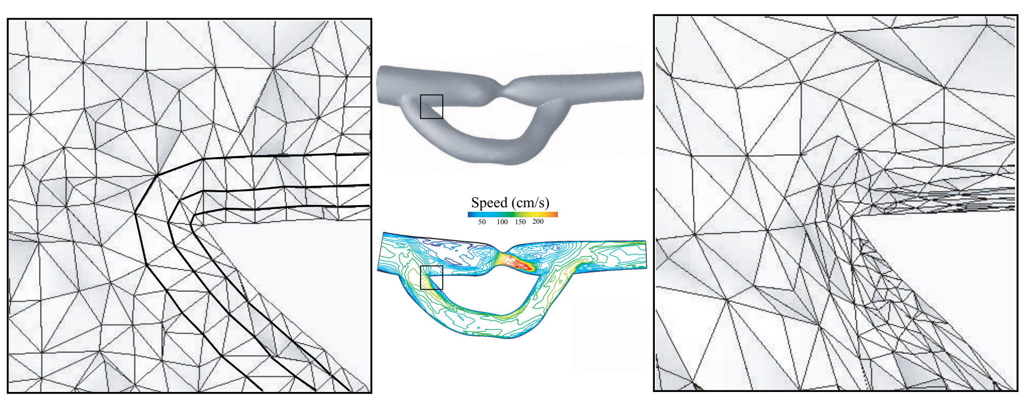

Fig. 3. Advancing layers and anisotropically adapted mesh of a porcine aortic bypass model.

advantages of both the advancing layers method and the anisotropic adaptation by introducing a methodology in which the mesh is modified according to the demands of the computed size field and at the same time maintains most of the structured nature of the advancing layers mesh in the close proximity of the walls.

4.3 Hybrid Advancing Layers-Anisotropic Adaptation Method

The proposed algorithm enables the adaptive procedures to maintain structured and graded elements near the walls for accurate prediction of wall quantities (like WSS). The initial adaptation cycle is performed on a mesh that already carries an advancing layers mesh on no-slip boundaries. Subsequent mesh adaptation preserves the layer structure normal to the walls while at the same time incorporating desired element sizes in different directions as indicated by the *a posteriori* size field information. The BL elements are viewed as a product of a surface mesh (2D) and a thickness mesh (1D) as depicted in Fig. 4. To preserve the structure of the mesh along the normals of the walls the adaptive procedure is divided into two steps: surface adaptation and thickness adaptation. The mesh composed of triangles located at the top of each layer will be referred to as a *layer surface*, see Fig. 4, while the lines orthogonal to the wall composed of edges are called *growth curves*. This two step adaptive

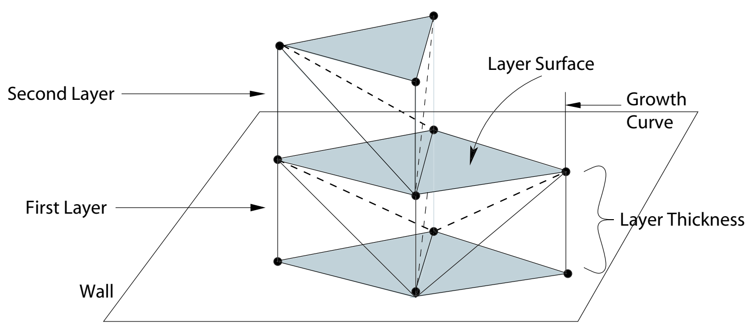

Fig. 4. Conceptual decomposition of a BL element generated by advancing layers method.

procedure is driven by the computed mesh metric field. The mesh metric field at any point on a wall is decomposed into two components: a component on the layer surface (referred to as planar part) and a normal component along the layer thickness, see Fig. 5. This decomposition procedure can be performed similarly to the metric alignment procedure presented in section 3.5. Here, the normal component is composed of size h_n along the normal and the planar part is composed of the projected vectors ($\boldsymbol{p}_{t1}$ and $\boldsymbol{p}_{t2}$), and corresponding sizes (h_{t1} and h_{t2}), on the tangential plane. With this information in hand, the decision to apply any mesh modification procedure on a layer surface will be governed by the planar part of the mesh metric tensor and any change in the layer thickness will be based on the normal component. Basic mesh modification operations, like edge split, edge collapse, node movement etc. [2,31],

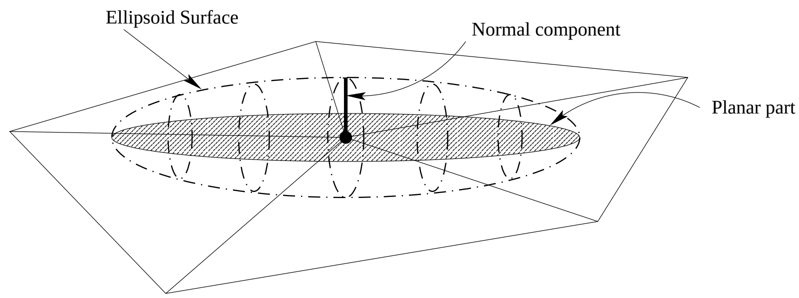

Fig. 5. Conceptual decomposition of a mesh metric tensor.

can be applied to perform these steps.

The edges of a boundary layer element can be classified into three categories, as depicted in Fig. 6:

- *Layer edge*: All the edges of a BL element that have their nodes on the same layer surface.
- *Growth edge*: Shortest edge, along the surface normal, of a BL element that has its nodes on different layer surfaces.
- *Diagonal edge*: All the remaining edges of a BL element (that essentially tetrahedronize the BL prisms).

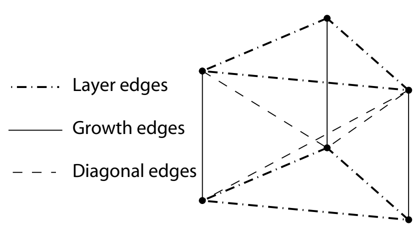

Fig. 6. Classification of edges of a boundary layer element.

To perform adaptation on a layer surface only *layer edges* will take part in the modification process in the plane whereas to change the thickness of layers only *growth edges* will be split (or collapsed) and/or their lengths will be adjusted through node movement. It is possible to carry out both of these operations in a way that results in graded elements in the normal direction. The existence of *diagonal edges* (see, Fig. 6) makes the process tedious, but considering the inherent structure of triangular prisms enables one to simplify the process. The surface adaptation is made possible with the help of three basic mesh modification operations:

(1) **Edge Split**: An edge split operation will split a *layer edge* into two *layer edges*. Fig. 7(a) shows the initial and final mesh topology.
(2) **Edge Collapse**: An edge collapse operation will collapse a *layer edge*.

Fig. 7(b) shows the initial and final mesh topology.

(3) **Edge Swap**: An edge swap operation will swap a *layer edge*. Fig. 7(c) shows the initial and final mesh topology.

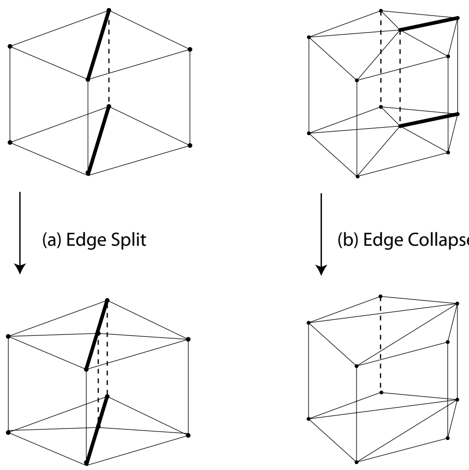

Fig. 7. Mesh topology before (top) and after (bottom) mesh modification : (a) edge split, (b) edge collapse and (c) edge swap.

In all the operations, basic geometric and topological validity checks must be carried out (see appendix A in [42] for details).

With the idea of working with triangular BL prisms, a mesh modification operation can be carried out on any layer surface and propagated through all the layers as shown in Fig 8(a). Node movement can be applied to change the layer thickness while maintaining the number and topology of layers. To introduce more structured layers of elements *growth edges* can be subdivided to create new nodes and in turn layers, see Fig. 8(b). After carrying out all the mesh modification operations boundary layer prisms can be tetrahedronized (see, [11]). In what follows we sketch the algorithm by demonstrating the major

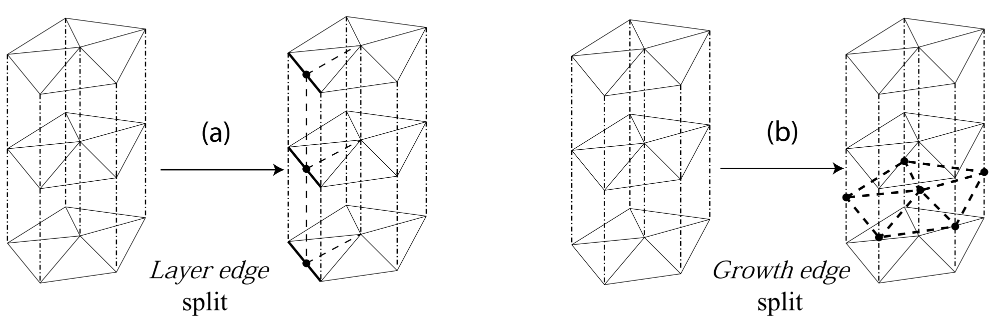

Fig. 8. Mesh modification applied on boundary layer prisms.

steps with the help of an example. Fig. 9 shows two sections of a clip plane through an advancing layers mesh together with ellipsoids representing the computed mesh metric field at a selected number of nodes. The mesh metric field has been computed as described in section 3. We should note that the metric field has been obtained on a mesh that only has about 13K nodes, a

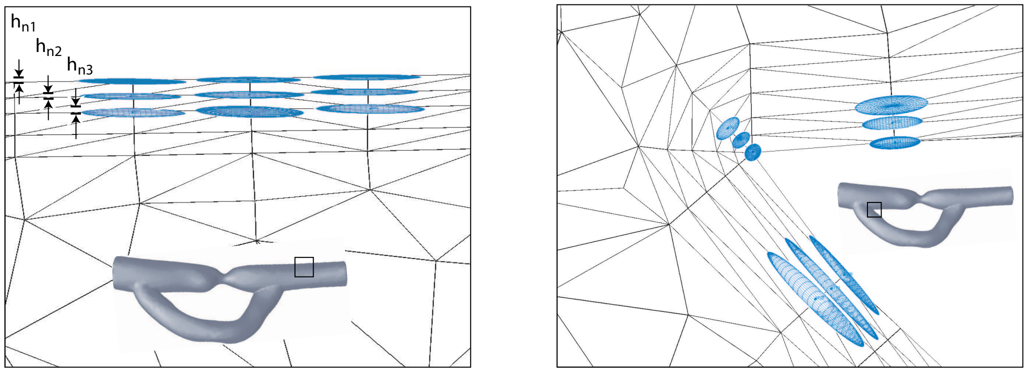

Fig. 9. Desired mesh metric tensors on a set of nodes of an advancing layers mesh : (a) simple case (left) and (b) corner case (right).

number far too small to expect sufficiently accurate flow results, not to mention second order field derivatives and their limited near wall reconstructability, on which the metric field is based. Nevertheless, it is representative of a mesh that one might start an adaptive computation from and is adequate to identify a number of items that suggest a mesh modification in a consistent manner, i.e.:

- Normal to wall distances of nodes may change significantly in a subsequently adapted mesh.
- While the thickness of the initial BL mesh is almost uniform, the modified mesh may feature a more significant gradation in normal direction (this point is more obvious when considering Fig. 9(b)).
- The initial element lengths parallel to the wall are too big, the modified mesh will have smaller element sizes in that direction.
- The deviation of the principal direction representing the largest eigenvalue (and thus responsible for the normal spacing) from the surface normal is small but does exist due to numerical errors.
- Further adaptation steps will render a more accurate mesh metric field computation possible.

Care is necessary when performing node movement since the desired normal sizes are dependent on the location of the nodes and thus become invalid if associated with a node that has been moved. Therefore, we parameterize growth curves such that the requested nodal spacing along a growth curve can be defined in terms of its parametric coordinates s, i.e., $h_n(s)$. This can be achieved by interpolation of the nodal values along a growth curve or by determining a user-defined function based on geometric or exponential growth rate. The new nodal locations of all the nodes on a given growth curve can be determined by sequentially querying the function $h_n(s)$.

5 APPLICATION TO BLOOD FLOW SIMULATION

This section consists of two parts. The first part demonstrates the application of the anisotropic adaptive procedure developed in section 3. Here, we compare the results obtained on adapted meshes based on two different strategies, one based on average flow and one based on mesh metric intersection, incorporating metric alignment at the walls. These results are also compared to those obtained on a series of uniform meshes in order to assure their convergence and to quantify the efficiency of our adaptive procedure in the computation of wall shear stresses. The example considered involves pulsatile flow in a 3D vessel with a symmetric bifurcation that serves as a prototype problem for blood flow simulation.

In the second part of this section we support our contention that a hybrid approach, which incorporates advantages of both the generalized advancing layers method and anisotropic adaptivity, is required to obtain efficient and accurate WSS computations, as indicated in section 4. To this end, we present results for steady flow in a channel and a straight vessel with a steep velocity gradient near the walls. We compare WSS values obtained on meshes that possess structure near the walls to the ones computed on an anisotropically adapted mesh.

5.1 Anisotropic Mesh Adaptation

We demonstrate the anisotropic method presented in section 3 on a model which bifurcates into symmetric branches as shown in Fig. 10. The model is

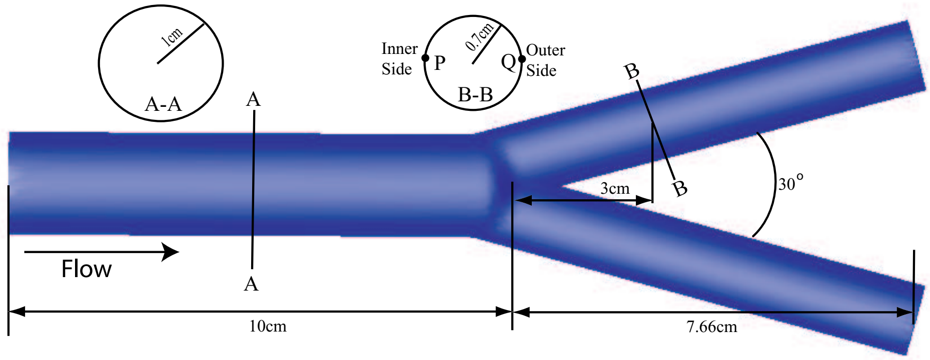

Fig. 10. Model of a blood vessel with a symmetric bifurcation

used for convergence analysis for our method. More physiologically realistic models and simulations using anisotropic adaptivity can be found in [17]. The time varying inflow boundary condition at the left end is assumed to be a

Womersley profile [43], with Womersley number $\alpha = 5.6$ and time period $t_p = 5s$, for which the flow rate is depicted in the inset of Fig. 11. We apply zero velocity (no-slip) boundary conditions on the vessel walls and zero natural

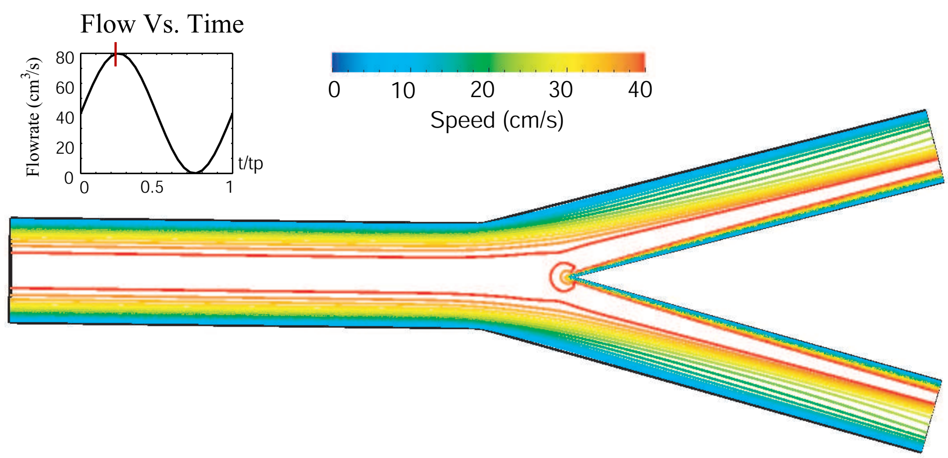

Fig. 11. Isolines of flow speed on a clip plane in a model with a symmetric bifurcation. The inset shows the Womersley inlet flow rate along with the instant the flow profile corresponds to.

pressure at the traction-free outlet. In this case, the viscosity and the density are assumed to be $\mu = 0.04 dyn\ s/cm^2$ and $\rho = 1 g/cm^3$, respectively.

We carry out simulations on a series of uniform meshes with varying mesh density and on meshes that have been anisotropically adapted. The uniform meshes consist of approximately 97K, 205K and 594K nodes, respectively, whereas the adapted meshes have approximately 15K nodes. The simulations were performed for two cycles to obtain a periodic flow and thus the results for the second cycle are presented here. Each cycle was divided into 500 time steps with a constant time step size of $0.01s$. The simulations on the finest uniform and the adapted meshes with 1000 time steps per cycle show no significant difference when compared to the ones obtained with 500 time steps per cycle, which ensures that the temporal errors are smaller than those due to the spatial discretization.

In this case, the intersected metric field was constructed by considering 25 equidistributed instants over the cycle, sufficient to capture the transient flow behavior. We first mention the common features that both the adapted meshes exhibit. A clip plane of the adapted meshes along the flow illustrates the effect of the mesh modification procedures, see Fig. 12. Note that the clip planes shown are not actual planes, rather they are a collection of the mesh faces cut by the physical plane. All the newly created boundary nodes during adaptation have been snapped to the model surface. We observe that anisotropic elements aligned with the flow are created. While in the upper part of the ves-

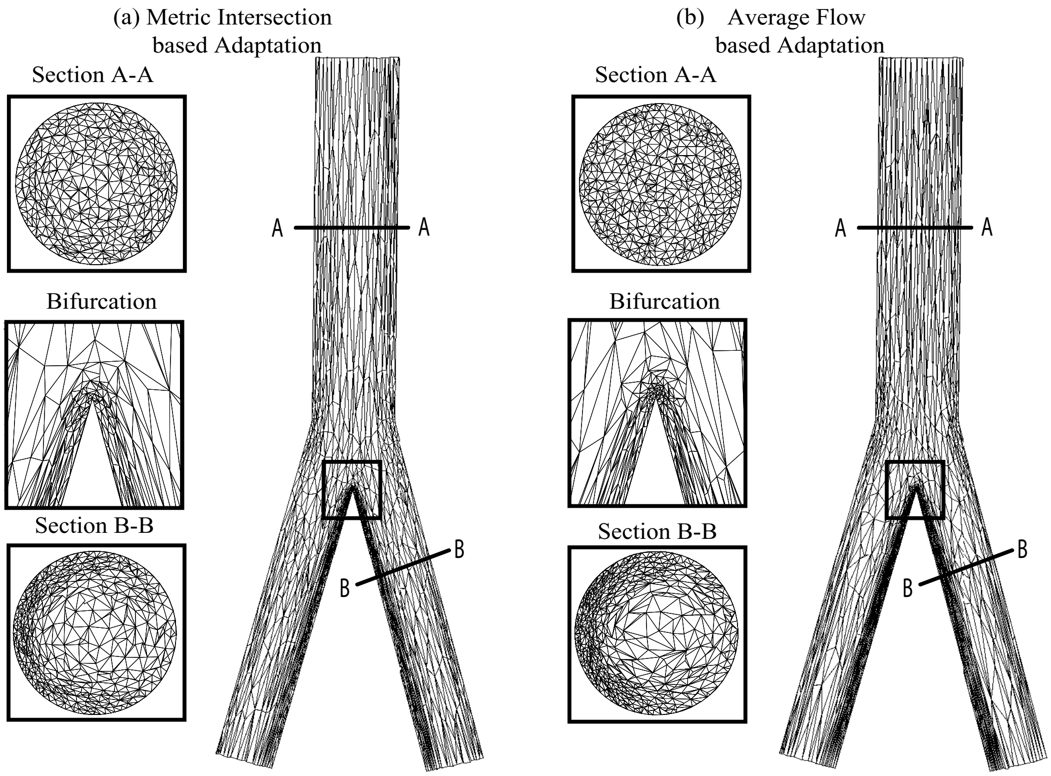

Fig. 12. Clip plane through anisotropically adapted meshes of a vessel with a symmetric bifurcation (the windows correspond to zooms).

sel anisotropy in the plane perpendicular to the flow is less distinct, see section A-A, the mesh in branches exhibit significant anisotropy in the plane perpendicular to the flow especially near the inner side of the vessel walls where the velocity gradients are steep, see section B-B. We can identify azimuthal anisotropy for section B-B where the mesh resolution is varying in both the azimuthal and radial direction. The instantaneous flow field, as depicted in Fig. 11, makes the above observations more obvious. There are significant changes in both the adapted meshes close to the bifurcation. The element sizes in this portion are small but isotropic for both meshes (see the center zoom windows in Fig. 12 (a) and (b)), reflecting the fact that the solution behavior is singular around the bifurcation. This example shows the capability of our adaptive procedure to handle situations with arterial branching, i.e., it suitably adapts the mesh for cases with both isotropic and anisotropic flow behavior.

The two different procedures for determining the mesh size field can result in different resolution of transient flow features. Fig. 13 shows the mesh in the branches for the two cases. Here we observe a portion of surface mesh for the inner and outer side of a branch (surface meshes are similar for the other branch due to symmetry of the problem and thus are not shown). Note that the elements along the flow direction are much longer in the adapted mesh that is based on the average flow field. This is due to the fact that the flow is not fully developed after the bifurcation and the pulsatile nature of the flow further adds to the complexity in the problem leading to a time dependent axial variation in the velocity field within the branches. Mesh adaptation based on the average flow scenario does not correctly account for this transient flow feature whereas the one based on mesh metric intersection is more effective.

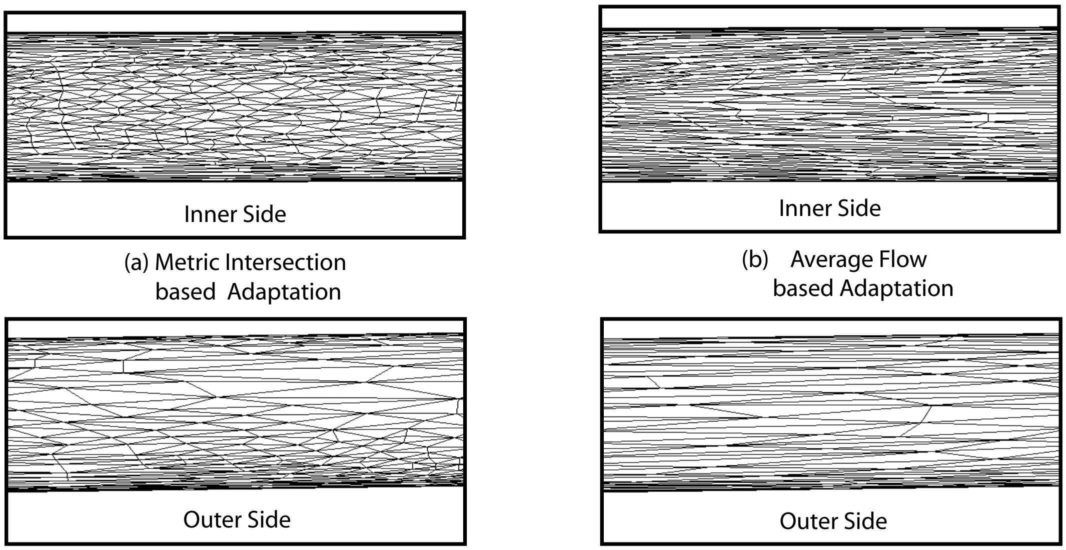

Fig. 13. Surface of anisotropically adapted meshes near section BB of the bifurcating vessel.

To evaluate the efficiency of our adaptive procedure we first obtain results on a series of uniform meshes which have converged and then use the most converged result for the purpose of comparison. We select section B-B of one of the branches as the location where the adaptive procedure plays a significant role to capture the flow features. The WSS values for this location are not constant along the circumference at any given instant as the flow profile is varying in the azimuthal direction. In Fig. 14 the plot on the left shows results on uniform meshes along with the one obtained on an adapted mesh based on the intersected metric field whereas the plot on the right compares results obtained on adapted meshes based on different strategies with the one computed on the finest uniform mesh. Analyzing the plot on the left indicates that the anisotropic adaptivity is particularly well suited to resolve the high shear region near the inner side of the vessel branch where fluctuations even of the finest uniform mesh are comparatively high. In the right plot we observe that the mesh adapted based on the average flow scenario yields significantly higher fluctuations as compared to the metric intersection procedure, especially near the inner (i.e., close to 90 degrees) and outer (i.e., close to 270 degrees) side of section B-B. Fig. 14 shows that the metric intersection based anisotropic adaptivity is capable of obtaining solutions that are as accurate as uniform meshes with an order of magnitude fewer *dofs* (around 15K nodes

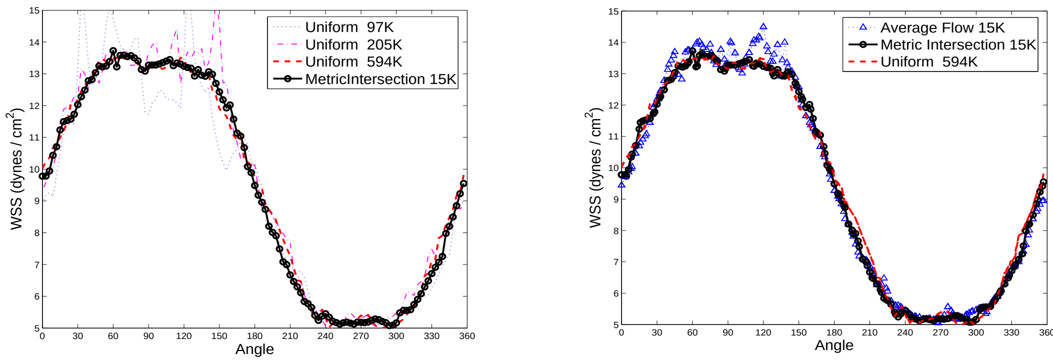

Fig. 14. WSS values along the circumference at section B-B in a vessel with a symmetric bifurcation. The left figure confirms that the anisotropic adaptivity utilizing metric intersection achieves the converged solution with only 15K nodes. The right figure indicates the improvement achieved by the metric intersection compared to the average flow based metric.

were used in the anisotropically adapted cases which compare favorably to the uniform case with nearly 600K nodes).

As this is a time varying flow it is also interesting to see the convergence of the temporal behavior with improved spatial resolution. We have selected two points, P and Q, that lie on the inner and outer side, respectively, of section B-B (as depicted in Fig. 10). The first observation from the plots in Fig. 15 is that the results are significantly smoother in the time domain than in the spatial domain shown in Fig. 14. This illustrates that the spatial noise associated with recovering a flux quantity does not globally pollute the solution in time, suggesting that the primary fields (velocity and pressure) remain unaffected. We observe in the plots on the left column of Fig. 15 that the solution has converged on uniform meshes and that the adapted mesh which is based on metric intersection is able to attain the converged solution. The plots on the right demonstrate that the results obtained on the adapted mesh based on the average flow field do not yet yield accurate results especially in intervals near the peak flow where the values are approximately off by 8-10 percent at point P. For the same number of nodes (approximately 15K), the metric intersection procedure matches the finest (converged) uniform mesh result. We finally want to reiterate that the WSS is a derivative field quantity and therefore is subjected to a lower convergence rate than the primary field quantities. To reproduce accurate spatial and temporal WSS values for pulsatile flow simulations therefore is particularly demanding.

5.2 Anisotropic Adaptation with Boundary Layer Mesh

In this subsection we present results that show the impact of the mesh structure close to the vessel walls on WSS computation. We compare results that

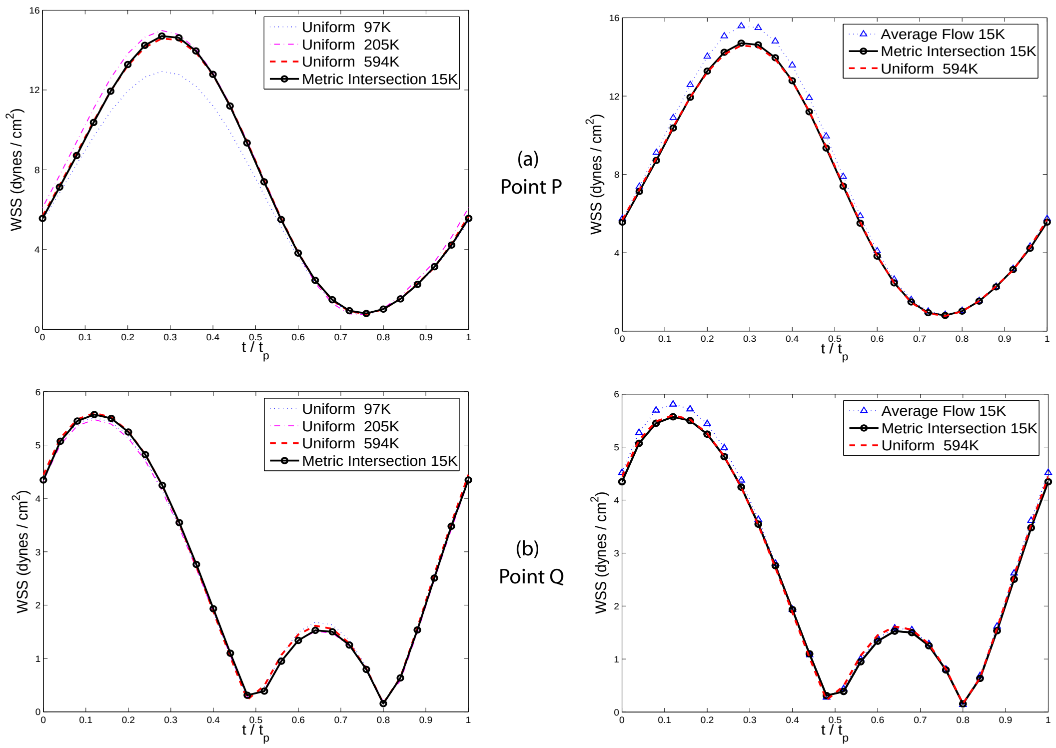

Fig. 15. WSS values with time at points P and Q in a vessel with a symmetric bifurcation (also see caption of Fig. 14).

are computed after having applied two different meshing strategies, one in which meshes are obtained by performing a complete anisotropic mesh adaptation process and another in which meshes are obtained by constraining the structured layer of elements for one (or two) layer(s) near the walls in the process of mesh adaptation. As the problems considered in this section involve stationary flow we perform adaptation based on the steady-state numerical solution. The meshes in the second case are generated by a sequence of steps that can be described as follows: first, the anisotropic adaptive strategy is applied, secondly, the interior volume mesh is removed, leaving only the surface mesh, thirdly, a boundary layer mesh with specific attributes is grown on the remaining surface mesh, and finally, the resulting mesh is subjected to the anisotropic adaptive procedure again, while constraining a defined number of the layer(s) along the boundary. Therefore, the meshes for each of the cases described above exhibit identical surface meshes and similar mesh resolution along the normals. In doing so, we are, to a limited extent, mimicking a hybrid approach proposed in section 4. We should note that the sequence of steps followed in the second case does not allow for adjustment of sizes in normal-to-wall direction.

First we apply the procedure to a simple case of high shear flow between parallel plates. In the second case, we consider a similar flow in a straight cylindrical vessel. In both the cases, the computation is performed for several time steps until a well converged steady-state solution has been obtained.

5.2.1 Channel Flow

In this example, we consider channel flow as a benchmark problem with a steep velocity near a wall, unaffected by wall curvature. The inlet flow profile is taken to be:

$$u = ((25(1 - |y|))^{-2} + ((1 - |y|)^{1/7})^{-2})^{-\frac{1}{2}}, \tag{27}$$

where y (≤ 1) is the distance from the center plane of the channel. The viscosity is set to a low value of $\mu = 10^{-5} dyn\ s/cm^2$ to avoid significant diffusion of the flow profile, and the density is assumed to be $\rho = 1g/cm^3$. The model is depicted in Fig. 16 along with an inset that shows the inlet flow profile. The profile based on the one-seventh power law is chosen to allow for highly varying second derivatives along the height of the channel, which adequately reflects the situation that we face in real physiological flows, see the instantaneous flow field in Fig. 11, and more detailed in [17]. We compare simulation

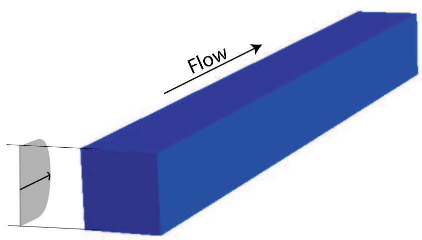

Fig. 16. Model of a channel with inlet flow profile.

results obtained on three different meshes. Fig. 17 shows the three meshes used: the first one is a completely adapted mesh and the others have structured elements frozen (i.e., not subjected to any mesh modification) for one and two layer(s) near the walls. The windows show zooms of the meshes close to the wall. As before, the adaptation is based on the Hessian strategy. As the domain is a polyhedron there is no geometric model approximation error. This case enables the isolation of the mesh sensitivity in the post-processing step of WSS computation. We show WSS values on the upper surface of the channel at different locations along the length, which remain nearly constant due to the artificially small diffusion, in Fig. 18. Table 1 provides the mean values along with the standard deviations of WSS for locations near the outflow, i.e., farther away from the artificial inflow. Based on the inlet profile, the exact value of the WSS is $2.5 \times 10^{-4} dynes/cm^2$.

We observe that oscillations of WSS are reduced by an order of magnitude with the use of structured layer(s) of elements near the walls. Most of the

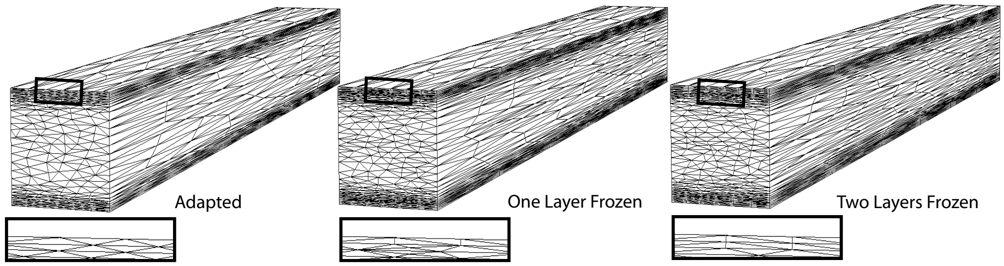

Fig. 17. Three different meshes used for a channel (the windows correspond to zooms).

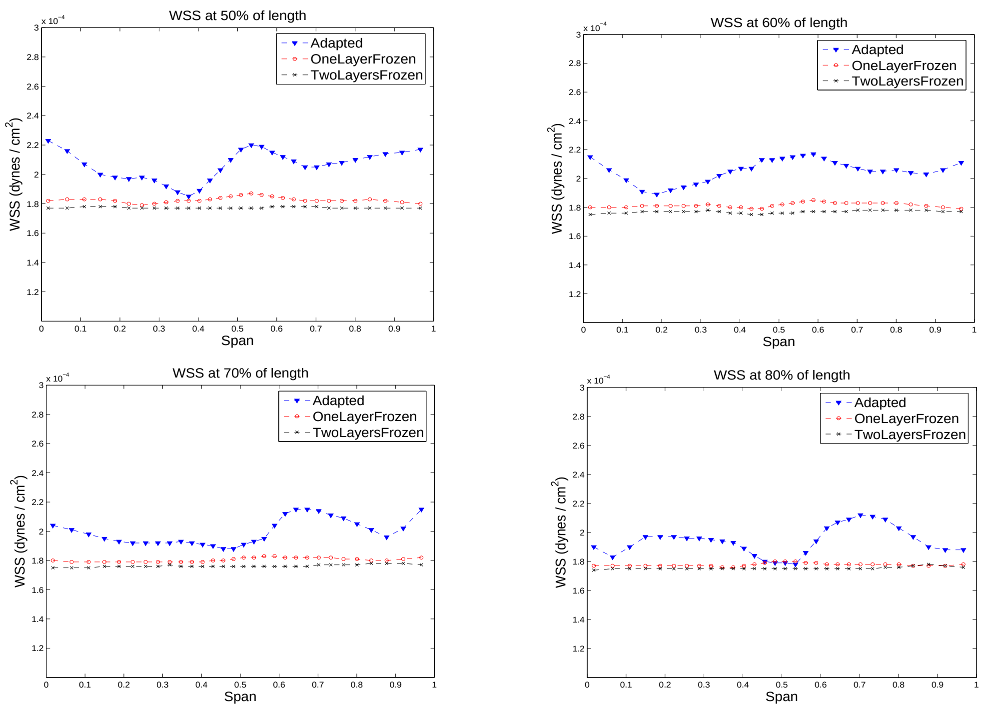

Fig. 18. WSS values along the span on upper surface at different downstream locations for a channel.

fluctuations even diminish when only one structured layer of elements is used. This observation is true for all the locations that are shown, noting that the differences between the one and two structured layer(s) meshes vanish quickly with increasing distance downstream. The results clearly demonstrate that WSS computation is sensitive to the mesh quality close to the walls and shows that WSS computations can be significantly improved when using structured layer(s) of elements.

Table 1
WSS mean values (in $dynes/cm^2$) and standard deviations (σ) for high shear flow in a channel.

Mesh type	Mean WSS	σ
Adapted	1.9975e-4	1.9292e-5
One Layer Frozen	1.7931e-4	3.8245e-6
Two Layers Frozen	1.7559e-4	1.9011e-6

5.2.2 Cylindrical Vessel Flow

In this example, we consider a high shear flow in a straight cylindrical vessel. The value of the viscosity is set to $\mu = 10^{-5} dyn\ s/cm^2$ and the density is assumed to be $\rho = 1g/cm^3$. The model is depicted in Fig. 19 along with an inset that depicts the inlet flow profile, which is an artificial steep flow profile similar to (27), where y has to be replaced by the radial distance. As in

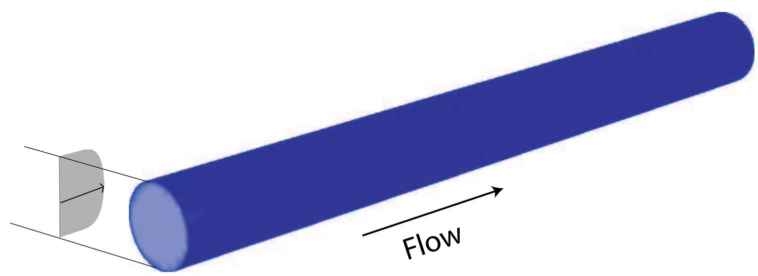

Fig. 19. Model of a vessel with inlet flow profile.

the previous example we obtain simulation results on three different meshes (see Fig. 20). We show the computed WSS values along the circumference of the vessel at different downstream locations in Fig. 21. Table 2 provides the mean values along with the standard deviations of WSS for locations near the outflow of the vessel, i.e., away from the artificial inflow.

Table 2
WSS mean values (in $dynes/cm^2$) and standard deviations (σ) for high shear flow in a straight vessel.

Mesh type	Mean WSS	σ
Adapted	1.9139e-4	1.9857e-5
One Layer Frozen	1.8551e-4	1.1200e-5
Two Layers Frozen	1.7989e-4	6.1007e-6

Similar to the case of the flat channel we observe that the oscillations of computed WSS significantly decrease (by a factor of around four) with the help of structured layer(s) of elements near the walls. Note that the fluctuations do

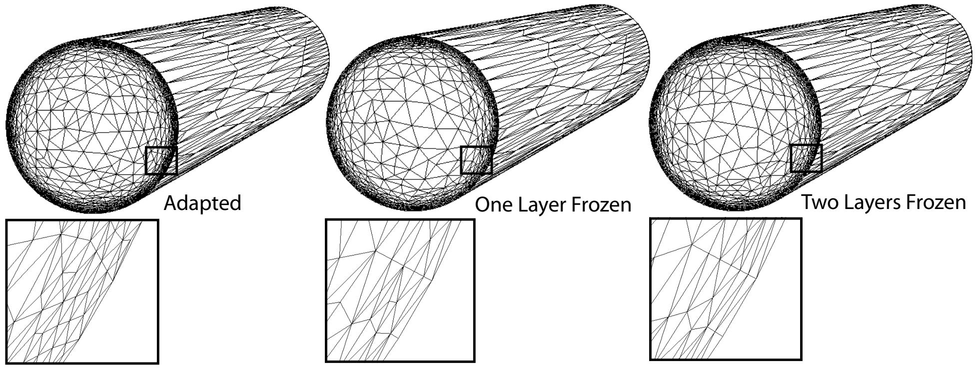

Fig. 20. Three different meshes used for a cylindrical vessel (the windows correspond to zooms).

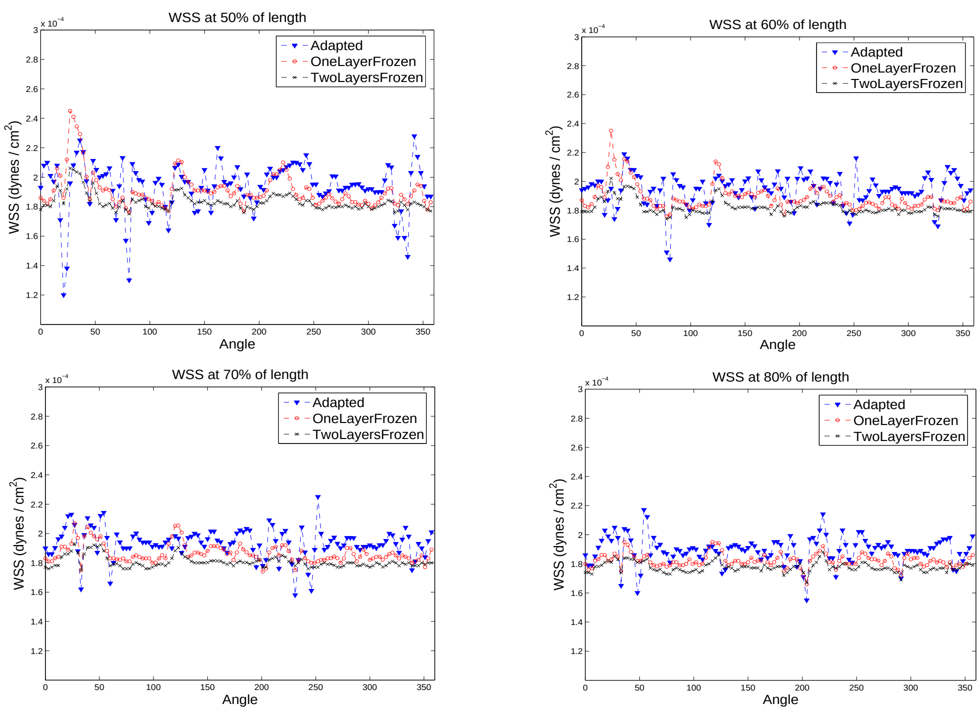

Fig. 21. WSS values along the circumference at different downstream locations for vessel.

not completely vanish when using structured layers, owing to the fact that both flow and shear stress computation are also sensitive to the approximation of the geometric model (introduced due to linear straight sided elements). Again, the oscillations dampen out in the downstream direction. This example shows that structured layer(s) of elements near the walls are required to improve the WSS computation substantially in vessel geometries with curved boundaries.

6 CONCLUSIONS AND FUTURE WORK

In this article, we have presented adaptive meshing procedures for computational hemodynamics. The method we have introduced is based on anisotropic mesh adaptivity dictated by directional error indicators. These are used to construct a mesh metric field that yields information on the local mesh resolution desired in different directions. Mesh adaptation governed by such a mesh metric field results in highly anisotropic meshes well aligned with the flow features leading to substantial computational savings. We discussed two different strategies to obtain a mesh metric field that can be used to perform mesh adaptation for the whole cardiac cycle. We have also proposed a hybrid method by which anisotropic adaptivity and the structured nature of advancing layers meshing is utilized to further improve the accuracy of blood flow simulations, in particular computation of wall shear stress.

We have demonstrated the efficiency of our adaptive procedure, based on a metric intersection algorithm together with metric alignment at no-slip boundaries, by applying it to the simulation of pulsatile flow in a vessel with two symmetric branches. We showed that the adapted mesh based on an average flow scenario is not able to properly account for the transient flow features and therefore does not yield accurate wall shear stress values. We obtained gains of around one order of magnitude in terms of degrees of freedom when our method is applied. This serves as a first step to perform accurate blood flow simulations in real patient-specific geometries which would otherwise not be possible within a reasonable time due to limited computational resources.

We have demonstrated that meshes with structured layers of elements at the walls lead to better wall shear stress computations. We observed that the fluctuations of the values are higher by one order of magnitude on meshes without structured layers of elements in the case of channel flow. The fluctuations were approximately quadruple in the case of pipe flow for similar mesh resolution in the normal direction to the walls. This clearly supports our proposed methodology to use a hybrid adaptive procedure that combines anisotropic adaptivity with a generalized advancing layers method.

The current status of adaptive procedures shows that although these procedures have been successfully applied for many interesting problems in various areas of research, there are still open issues. These issues have to be addressed to design adaptive procedures applicable to more challenging problems, with complex geometries, possessing different degrees of anisotropy in the solution characteristics, over the spatial and temporal domain. Automatically obtaining a suitable mesh for different quantities of physical interest (like wall shear stress) not only requires focused effort to develop more sophisticated adaptive meshing techniques but also needs more stringent and dependable goal-oriented error estimation that can provide the necessary directional information. Therefore, efficient and reliable large scale viscous flow computations on geometries, like the human arterial system, deserve careful investigations to define the objectives of the adaptive procedures.

Acknowledgments

We gratefully acknowledge the support of this work by NSF grant ACI-0205741. This work was facilitated through an allocation of advanced computing resources by NPACI (NRAC program) through the support of the National Science Foundation. We would also like to thank Frédéric Alauzet (INRIA France) for helpful suggestions in this work. The solutions presented herein made use of the linear algebra solution library provided by AcuSim Software.

References

[1] C. A. Taylor, T. J. R. Hughes, C. K. Zarins, Finite element modeling of blood flow in arteries, Comp. Meth. Appl. Mech. Engng. 158 (1998) 155–196.

[2] X. Li, M. S. Shephard, M. W. Beall, 3D anisotropic mesh adaptation by mesh modifications, Comp. Meth. Appl. Mech. Engng. 2005, submitted.

[3] R. C. Almeida, R. A. Feijóo, A. C. Galeão, C. Padra, R. S. Silva, Adaptive finite element computational fluid dynamics using an anisotropic error estimator, Comp. Meth. Appl. Mech. Engng. 182 (2000) 379–400.

[4] G. C. Buscaglia, E. A. Dari, Anisotropic mesh optimization and its application in adaptivity, Int. J. Numer. Meth. Engng. 40 (1997) 4119–4136.

[5] M. J. Castro-Diáz, F. Hecht, B. Mohammadi, O. Pironneau, Anisotropic unstructured mesh adaption for flow simulations, International Journal of Numerical Methods in Fluids 25 (1997) 475–491.

[6] W. G. Habashi, J. Dompierre, Y. Bourgault, D. Ait-Ali-Yahia, M. Fortin, M.-G. Vallet, Anisotropic mesh adaptation: towards user-independent, mesh-independent and solver-independent CFD. Part I: general principles, International Journal of Numerical Methods in Fluids 32 (2000) 725–744.

[7] P. J. Frey, F. Alauzet, Anisotropic mesh adaptation for CFD computations, Comp. Meth. Appl. Mech. Engng. 2005, submitted.

[8] C. C. Pain, A. P. Umpleby, C. R. E. de Oliveira, A. J. H. Goddard, Tetrahedral mesh optimisation and adaptivity for steady-state and transient finite element calculations, Comp. Meth. Appl. Mech. Engng. 190 (2001) 3771–3796.

[9] J. F. Remacle, X. Li, M. S. Shephard, J. E. Flaherty, Anisotropic adaptive simulation of transient flows using Discontinuous Galerkin methods, Int. J. Numer. Meth. Engng. 62 (2005) 899–923.

[10] X. Li, M. S. Shephard, M. W. Beall, Accounting for curved domains in mesh adaptation, Int. J. Numer. Meth. Engng. 58 (2003) 247–276.

[11] R. V. Garimella, M. S. Shephard, Boundary layer mesh generation for viscous flow simulations, Int. J. Numer. Meth. Engng. 49 (2000) 193–218.

[12] Y. Ito, K. Nakahashi, Unstructured mesh generation for viscous flow computations, in: Proc. 11th Internatinal Meshing Roundtable, Ithaca, NY, USA, 2002.

[13] K. E. Jansen, M. S. Shephard, M. W. Beall, On anisotropic mesh generation and quality control in complex flow problems, in: Proc. 10th Internatinal Meshing Roundtable, Newport Beach, CA, USA, 2001.

[14] A. Khawaja, Y. Kallinderis, Hybrid grid generation for turbomachinery and aerospace applications, Int. J. Numer. Meth. Engng. 49 (2000) 145–166.

[15] R. Löhner, J. Cebral, Generation of non-isotropic unstructured grids via directional enrichment, Int. J. Numer. Meth. Engng. 49 (2000) 219–232.

[16] S. Prakash, C. R. Ethier, Requirements for mesh resolution in 3D computational hemodynamics, J. Biomech. Eng. 123 (2001) 132–144.

[17] J. Müller, O. Sahni, X. Li, K. E. Jansen, M. S. Shephard, C. A. Taylor, Anisotropic adaptive finite element method for modeling blood flow, Comp. Meth. Biomech. Biomed. Eng. 2005, submitted.

[18] C. H. Whiting, K. E. Jansen, A stabilized finite element method for the incompressible Navier-Stokes equations using a hierarchical basis, International Journal of Numerical Methods in Fluids 35 (2001) 93–116.

[19] A. N. Brooks, T. J. R. Hughes, Streamline upwind / Petrov-Galerkin formulations for convection dominated flows with particular emphasis on the incompressible Navier-Stokes equations, Comp. Meth. Appl. Mech. Engng. 32 (1982) 199–259.

[20] I. Vignon-Clementel, A. Figueroa, K. E. Jansen, C. A. Taylor, Outflow boundary conditions for three-dimensional finite element modeling of blood flow and pressure in arteries, Comp. Meth. Appl. Mech. Engng. 2005, accepted.

[21] L. P. Franca, S. Frey, Stabilized finite element methods: II. The incompressible Navier-Stokes equations, Comp. Meth. Appl. Mech. Engng. 99 (1992) 209–233.

[22] T. J. R. Hughes, L. P. Franca, G. M. Hulbert, A new finite element formulation for fluid dynamics: VIII. The Galerkin / least–squares method for advective–diffusive equations, Comp. Meth. Appl. Mech. Engng. 73 (1989) 173–189.

[23] K. E. Jansen, C. H. Whiting, G. M. Hulbert, A generalized-α method for integrating the filtered Navier-Stokes equations with a stabilized finite element method, Comp. Meth. Appl. Mech. Engng. 190 (1999) 305–319.

[24] F. Shakib, http://www.acusim.com.

[25] T. J. R. Hughes, The finite element method: Linear static and dynamic finite element analysis, Prentice Hall, Englewood Cliffs, NJ, 1987.

[26] T. J. R. Hughes, G. Engel, L. Mazzei, M. G. Larson, The continuous Galerkin method is locally conservative, Journal of Computational Physics 163 (2000) 467–488.

[27] P. M. Gresho, R. L. Sani, Incompressible Flow and the Finite Element Method, Wiley, New York, NY, 1998.

[28] M. Ainsworth, J. T. Oden, A Posteriori Error Estimation in Finite Element Analysis, John Wiley & Sons, New York, 2000.

[29] R. Verfürth, A Review of Posteriori Error Estimation and Adaptive Mesh-Refinement Techniques, Teubner-Wiley, Stuttgart, 1996.

[30] E. Bänsch, Local refinements in 2 and 3 dimensions, Impact of Comp. in Sci. and Engng. 3 (1991) 181–191.

[31] H. L. de Cougny, M. S. Shephard, Parallel refinement and coarsening of tetrahedral meshes, Int. J. Numer. Meth. Engng. 46 (1999) 1101–1125.

[32] P.-L. George, H. Borouchaki, P. Laug, An efficient algorithm for 3D adaptive meshing, Advances in Engineering Software 33 (2002) 377–387.

[33] P.-L. George, Tet meshing: construction, optimization and adaptation, in: Proc. 8th Internatinal Meshing Roundtable, South Lake Tao, CA, USA, 1999.

[34] X. Li, Mesh modification procedures for general 3-d non-manifold domains, Ph.D. thesis, Rensselaer Polytechnic Institute (Aug. 2003).

[35] G. Kunert, Toward anisotropic mesh construction and error estimation in the finite element method, Numer. Methods Partial Differential Equations 18 (2002) 625–648.

[36] P. G. Ciarlet, The finite element method for elliptic problems, North-Holland, Amsterdam, 1978.

[37] P. J. Frey, F. Alauzet, Anisotropic mesh adaptation for transient flows simulations, in: Proc. 12th Internatinal Meshing Roundtable, Santa Fe, NM, USA, 2003.

[38] T. Apel, M. Dobrowolski, Anisotropic interpolation with applications to the finite element method, Computing 47 (1992) 277–293.

[39] L. Formaggia, S. Perotto, New anisotropic a priori error estimates, Numer. Math. 89 (2001) 641–667.

[40] H. Borouchaki, P.-L. George, B. Mohammadi, Delaunay mesh generation governed by metric specifications. Part II. Applications, Finite Elements in Analysis and Design 25 (1997) 85–109.

[41] F. Alauzet, Adaption de maillage anisotrope en trois dimensions. applications aux simulations instationaires en mécanique des fluides, Ph.D. thesis, L'Université de Montpellier II (Sep. 2003).

[42] R. V. Garimella, Anisotropic tetrahedral mesh generation, Ph.D. thesis, Rensselaer Polytechnic Institute (May 1999).

[43] J. Womersley, Method for the calculation of velocity, rate of flow and viscous drag in arteries when the pressure gradient is known, J. Physiol. (London) 127 (1955) 553–563.